Electronic Supplementary Material (ESI) for Journal of Materials Chemistry A.
This journal is © The Royal Society of Chemistry 2022

Electronic Supplementary Information for

Thermodynamic guiding principles of high-capacity phase transformation materials for splitting H_2O and CO_2 by thermochemical looping

Shang Zhai[1,*], Joonhyun Nam[2], Gopalakrishnan Sai Gautam[3,†], Kipil Lim[4,5], Jimmy Rojas[1], Michael F. Toney[6], Emily A. Carter[3,7], In-Ho Jung[2], William C. Chueh[4,8,9], Arun Majumdar[1,8]

[1] Department of Mechanical Engineering, Stanford University, Stanford, CA 94305, USA.

[2] Department of Materials Science and Engineering, Seoul National University, Seoul, 08826, South Korea.

[3] Department of Mechanical and Aerospace Engineering, Princeton University, Princeton, NJ 08544, USA.

[4] Department of Materials Science and Engineering, Stanford University, Stanford, CA 94305, USA.

[5] Stanford Synchrotron Radiation Lightsource, SLAC National Accelerator Laboratory, Menlo Park, CA 94025, USA.

[6] Department of Chemical and Biological Engineering, University of Colorado Boulder, Boulder, CO 80309, USA.

[7] Office of the Chancellor and Department of Chemical and Biomolecular Engineering, University of California, Los Angeles, CA 90095, USA.

[8] Precourt Institute for Energy, Stanford University, Stanford, CA 94305, USA.

[9] Applied Energy Division, SLAC National Accelerator Laboratory, Menlo Park, CA 94025, USA.

[*] Corresponding author: shangz@stanford.edu

[†] Present address: Department of Materials Engineering, Indian Institute of Science, Malleshwaram, Bengaluru, Karnataka 560012, India.

Supplementary Text

1. Materials synthesis and quenching

Sol-gel synthesis was used for all $Fe_yCo_{1-y}O_x$ ferrites. Iron(III) nitrate nonahydrate (≥98%, Sigma-Aldrich) and cobalt(II) nitrate hexahydrate (≥98%, Sigma-Aldrich) were dissolved with the correct global Fe/Co stoichiometry in deionized (DI) water with the ratio of precursors:water = 1:4 by mass. EDTA (ethylenediamine tetraacetic acid, ACS, MP Biomedicals) and citric acid (≥99.5%, Sigma-Aldrich) were added to the solution with 60% and 75% of the total molar amount of metal ions, respectively. (For example, for 1 mole of metals in total, 0.6 mol EDTA and 0.75 mol citric acid would be added.) With 300 rpm stirring, ammonium hydroxide solution (28% - 30%, Fisher Chemical) was added until the pH = 11 and a dark solution formed. The resulting solution was stirred and heated on a hot plate at 200 °C for about 5 hrs (gelation). The spin bar was removed and the temperature was increased to 400 °C to dry the gel overnight, during which time foaming occurred and fluffy solid residues formed. The sample then was ground into powder, transferred to an alumina boat, and went through the following calcination under air in a box furnace: heating 10 °C/min until reaching 800 °C and 5 °C/min until reaching 1000 °C, held at the latter temperature for an hour, followed by cooling at 5 °C/min until reaching 800 °C and then natural cooling.

CTF 17/300 CARBOLITE and Lindberg/Blue M Mini-Mite tube furnaces were used as the reactor for quenching (**Fig. S4**). The former furnace was used for 1300 °C and the latter for 800 °C. Sol-gel synthesized samples were ground with a mortar and pestle into powder, underwent thermal reduction or CO_2 splitting conditions, and finally were quenched under Ar immediately. X-ray characterizations were done on such quenched samples. At the beginning of the experiment, 100 sccm ultra-high purity Ar or a CO_2 + CO mixture (the balance was Ar) was purged into the tube furnace at room temperature until the p_{O_2} sensor at the gas outlet showed the expected value, which we call purge gas p_{O_2}. The background p_{O_2} is 0.5~2×10^{-5} atm when purging pure Ar; the expected p_{O_2} for a CO_2 + CO mixture is calculated by the CO + (1/2)O_2 = CO_2 equilibrium at the sensor electrode temperature. The furnace then was ramped up to T_H or T_L at 5 °C/min and after the p_{O_2} stabilizes at the purge gas p_{O_2} ($log_{10}p_{O_2}$ error bar $\pm$ 0.2), typically taking 1~3 days, the

alumina boat containing the sample was pushed from the hot zone to the (actively) cooled upstream side of the furnace in 1 second. To achieve this, the Ar flow rate was increased to 300~600 mL/min to avoid back-flow from the atmosphere and then a long alumina rod was inserted into the tube through a downstream Ultra Torr fitting. This Ultra Torr fitting was previously plugged and tightened with a rod in it. After quenching, the long alumina rod was retracted and the Ultra Torr fitting was tightened again. After everything cools down, the quenched sample then was ground into powder with a mortar and pestle and stored in an Ar-filled glove box.

2. Elemental analysis

An inductively coupled plasma optical emission spectrometer (ICP-OES) of model Thermo ICAP 6300 Duo View Spectrometer was used to quantify bulk metal ratios in $Fe_{0.45}Co_{0.55}O_{x_1}$ and $Fe_{2/3}Co_{1/3}O_{x_2}$ ferrite samples quenched after reaching equilibrium. A blank solution was a hydrochloric acid solution at about 2% made from DI water and concentrated hydrochloric acid (37%, ACS reagent, Sigma Aldrich). Standard solutions were made by diluting the blank solution, dissolving iron(III) nitrate nonahydrate (≥98%, Sigma-Aldrich) and cobalt(II) nitrate hexahydrate (≥98%, Sigma-Aldrich) further by the blank solution. Four standard solutions contained respectively 3, 7.5, 15 and 30 mass ppm of each of Fe^{3+} and Co^{2+}, made by independently diluting the solution of nitrates instead of by sequential dilution. Ferrite samples were weighed and completely dissolved in 37% hydrochloric acid, and the resulting solution was diluted by the blank solution so that the concentration of Fe and Co were around 10 mass ppm. The results are shown in **Table S1**, which confirm that the synthesis and quenching processes were accurate to achieve the nominal metal ratios.

3. Thermogravimetric analysis (TGA)

TGA measurements were used to confirm accuracy of CALPHAD modelling of the x_1-T-pO_2 relation for $Fe_{0.45}Co_{0.55}O_{x_1}$. The thermodynamic equilibrium oxygen stoichiometry x_1 in

$Fe_{0.45}Co_{0.55}O_{x_1}$was measured by a TGA. The reference condition was chosen to be at 800 °C and an oxygen partial pressure p_{O_2} = 0.17 atm, around which x_1 stays exactly at 4/3, as confirmed by CALPHAD models and experiments [1]. In each set of TGA measurements, the original sample mass was measured and then the reference condition was applied until the equilibrium sample mass was reached. Afterwards, various conditions relevant to two-step thermochemical CO_2 splitting were measured, with temperatures spanning from 800 °C to 1300 °C and p_{O_2} from 10^{-14} atm to 10^{-3} atm. For each condition, equilibrium was achieved when neither the sample mass nor the p_{O_2} of gas exhaust was changing. The background p_{O_2} in the TGA was around 10^{-5} atm when purging pure Ar. For $p_{O_2} > 10^{-5}$ atm, the purge gas was a mixture of ultra-high purity argon (Ar) and O_2 balanced by Ar; for $p_{O_2} < 10^{-5}$ atm, the purge gas was a mixture of CO_2 and CO balanced by Ar. As **Figs. S1-S2** show, experimental data from the TGA confirmed the accuracy of the x_1-T-pO_2 curves from the CALPHAD model of $Fe_{0.45}Co_{0.55}O_{x_1}$.

Meanwhile, the thermodynamics of $Fe_{2/3}Co_{1/3}O_{x_2}$ has been measured extensively before and the results were summarized and included into the CALPHAD model [1].

4. CALPHAD-FactSage simulations

Accurate thermodynamic databases can be developed through the CALculation of PHAse Diagram (CALPHAD) methodology. All thermodynamic property data such as enthalpy, entropy, heat capacity, and Gibbs energy, and phase diagram data within a given system in the literature are collected and evaluated critically and simultaneously to obtain one set of consistent thermodynamic data for all the phases within the system depending on temperature, composition, and pressure. The stoichiometric solid and liquid phase can be determined easily by a classical thermodynamics Gibbs energy function. In the case of complex solid and liquid solutions, the thermodynamic model reflecting the solution structure should be used for the thermodynamic assessment in order to consider properly the configurational entropy of the solution. Then the

model parameters can be optimized based on the assessed thermodynamic and phase diagram data, which are stored in the database. Once the database is available, the unknown thermodynamic properties, phase diagram, and change in enthalpy and entropy of a system at a given temperature and gas condition can be calculated using thermodynamic software such as FactSage [2], with its Gibbs energy minimization routine.

The thermodynamic database for the M1-M2-O system where M1 and M2 = Al, Co, Cr, Fe, Mg, Ni, Mn, etc. containing spinel, rocksalt, and metal solid solution has been constructed systematically [1,3–7] and stored in the FactSage database [2]. In particular, the Gibbs energy of spinel solid solution was described using the two-sublattice compound energy formalism [8], considering the cation distribution between tetrahedral and octahedral sites in the spinel lattice, as well as vacancy formation in octahedral sites. Rocksalt solid solution was described using the one-sublattice random mixing model, considering the non-stoichiometry by the dissolution of Fe_2O_3, Cr_2O_3, Mn_2O_3, and Al_2O_3. Using the FactSage thermodynamic database, we calculated the phase diagram, phase composition, and all the thermodynamic properties of each phase as a function of the temperature and partial pressure of oxygen; **Figs. 1, 2B,** and **3** display the results. In addition, we calculated the cation distributions in the spinel and rocksalt phases, in order to derive the change in the configuration entropy in ferrites for the thermodynamic analysis in **Figs. 1** and **2B**.

Specifically, we used oxygen stoichiometry at various temperatures and p_{O_2} values from CALPHAD to calculate the thermodynamic equilibrium CO_2 splitting capacity of ferrites in the thermochemical looping cycle. For example, we calculated the equilibrium oxygen stoichiometry at T_H for a p_{O_2} of 10^{-5} atm. This corresponds to a situation where the reactor p_{O_2} at the end of the oxygen release step is at this given value. Similarly, the equilibrium oxygen stoichiometry was calculated at T_L for a range of $CO:CO_2$. Again, this corresponds to a situation where the reactor $CO:CO_2$ molar ratio is at this given value at the end of the CO production step. For example, $CO:CO_2$ = 1:400 has an equivalent p_{O_2} as $10^{-13.25}$ atm at T_L = 800 °C.

5. First-principles quantum mechanics calculations

We performed all spin-polarized density functional theory based calculations using the Vienna ab initio simulation package (VASP) [9,10] within the projector augmented-wave (PAW) formalism [11], using the PAW potentials [12] employed in our previous work [13,14]. We employed a Hubbard U [15] corrected strongly constrained and appropriately normed [16] (i.e., SCAN+U) [13] functional to treat the electronic exchange and correlation. Specifically, we applied the rotationally invariant [17] DFT+U scheme, along with optimal U values of 3.1 and 3.0 eV for the d electrons of Fe and Co, respectively [13,14]. We used a kinetic energy cut off of 520 eV to expand the plane wave basis, sampled them on a dense Γ-point-centered k-point mesh (spacing ≤ 0.025 Å^{-1}), and used a Gaussian smearing (width = 0.05 eV) to integrate the Fermi surface, consistent with our previous studies [13,14,18,19]. We chose a 520 eV kinetic energy cut off to reduce the computational costs of evaluating all the symmetry-unique displacements to estimate the vibrational entropy in the four rocksalt and spinel structures considered. Moreover, we found that increasing the kinetic energy cut off did not change the relative energies of displacements (of a given structure) nor did it remove any of the imaginary phonon modes. The energies and forces were converged to 10^{-5} eV/cell and |0.03| eV/Å during all bulk structure relaxations. The magnetic moments of Fe and Co were aligned ferromagnetically since the rocksalt and spinel phases under consideration are not expected to be antiferromagnetic under thermal reduction and CO_2 splitting conditions [20–22]. The initial lattice parameters of both the rocksalt and the spinel phases came from synchrotron X-ray diffraction, described in **Subsection 6 in Supplementary Text of Electronic Supplementary Information (ESI)**. Specifically, cubic lattice parameters of 4.26 Å, 4.27 Å, and 8.39 Å were used for the rocksalt at 800 °C and CO:CO_2 = 1:400 ($p_{O_2} = 10^{-13.25}$ atm), the rocksalt at 1300 °C and $p_{O_2} = 10^{-5}$ atm, and the spinel (at both conditions above), respectively.

Since the rocksalt and spinel phases are both disordered under the conditions considered in this work, i.e., random occupations of cation sites by different species, we generated special quasirandom structures (SQSs) [23] to mimic randomness in the octahedral (in rocksalt and spinel) and tetrahedral (spinel) sites. We used the Monte Carlo routines within the "icet" python package [24] to generate the SQSs. To keep computational costs at a tractable level, we used a $2 \times 2 \times 2$ supercell of the primitive rocksalt (a total of 32 cations and 32 oxygens) and the conventional spinel cell (24 cations+32 oxygens) to create SQSs. Thus, the least counts in composition for any species that we can describe in our structure models are 0.03125 (=1/32) within the octahedral

sites in the rocksalt, 0.0625 (1/16) within the octahedral sites in the spinel, and 0.125 (1/8) in the tetrahedral spinel sites. In principle, we have five cationic species, namely Fe^{2+}, Fe^{3+}, Co^{2+}, Co^{3+}, and vacancies (Va), that can occupy the octahedral site in rocksalt and both the octahedral and tetrahedral sites in the spinel. Hence, we obtained target compositions of the rocksalt and spinel phases from CALPHAD simulations corresponding to the thermal reduction and CO_2 splitting conditions. Subsequently, we generated SQSs whose compositions had the least error versus the target CALPHAD composition, while maintaining charge neutrality of the generated structures within the constraint of the least counts that our structural models can accommodate. For each SQS, we allowed structural rotations, considered correlations within pair clusters up to 6-8 Å and triplets up to 4 Å to increase the similarity (Q [25]) of the SQS with an ideal random configuration, and ran a minimum of 40,000 Monte Carlo steps to obtain the final structure (convergence of Q with Monte Carlo steps shown in **Fig. S5**). **Table S2** lists the resultant SQS compositions and their comparison to the target CALPHAD compositions, with the structure models displayed in **Fig. S6**.

The CALPHAD simulations indicated that the spinel phase had nearly negligible cation vacancies, while the rocksalt phase exhibited a maximum cation vacancy content of 10%. CALPHAD simulations did not indicate the presence of Co^{3+} ions in rocksalt phase. In the spinel phase, Co^{3+} occupancies are very small (between 10^{-4} and 0.013), so we neglected Co^{3+} in our subsequent calculations. CALPHAD originally gives compositions that are charge neutral, hence including a small amount of Co^{3+}. Overall, we have three constraints on our SQS models: 1) least count (minimum compositional variation that we can account for); 2) charge neutrality, and 3) sum of site-fractions being equal to 1 in any sub-lattice. Given these three constraints, the distributions we arrived at in **Table S2** were the most optimal ones that achieved charge neutrality while minimizing the absolute error in compositions against CALPHAD. For example, the Fe^{2+} and Fe^{3+} occupancies in the 800 ^{o}C rocksalt phase by SQS are inverted from CALPHAD, but that was the only way we could ensure charge neutrality and similar occupancies to CALPHAD.

Upon generating the two rocksalt and the two spinel SQSs, we performed SCAN+*U* bulk relaxations, allowing the structures to change their volumes, shapes, and ionic positions subject to corresponding symmetry constraints. Subsequently, we used the relaxed SQSs to calculate the phonon density of states (DOS) and the vibrational entropy as a function of temperature, similar

to previous literature [26,27]. Specifically, we calculated the real-space force constants from symmetry-unique finite atomic displacements, generated with the "phonopy" package [28] for all four structures. In total, we obtained 378, 366, and 336 unique displacements for the 800 °C rocksalt, 1300 °C rocksalt, and each spinel (800 °C and 1300 °C), respectively. For each atomic displacement, we performed a single-point SCAN+*U* calculation (i.e., no ionic/structural relaxation), with the total energies converged to 10^{-8} eV/cell. To accelerate the single-point calculations, we initialized the wavefunctions of the displaced structures from the corresponding bulk-relaxed SQS. **Fig. S3** displays the resultant phonon DOS for all four structures. Imaginary phonon modes exist for all structures, as indicated by "negative" frequencies in **Fig. S3**, which are likely a consequence of the presence of cation disorder and vacancies. The true ground states of the rocksalt and spinel phases at 0 K are likely to be highly ordered, antiferromagnetic, and devoid of cation vacancies, with deviations from such ground-state configurations likely to result in imaginary phonon modes. Given our constraints on computational cost and structural model, it is impossible to avoid getting the imaginary phonon modes. Hence, we treat the imaginary modes as spurious and neglect their contribution in the eventual calculation of the vibrational entropy. For a given rocksalt or spinel structure, we obtained the vibrational entropy per f.u., i.e., MO and $M_{0.75}O$ in rocksalt and spinel, respectively, based on the thermodynamic formalism described in phonopy [28] documentation, a software package used to post-process phonon calculations. Note that the vibrational entropy per f.u. as defined above is the same as the vibrational entropy per O. Given the vibrational entropy (per O) of the rocksalt and spinel phases at a given temperature, the vibrational entropy per mole metal of the entire solid phase, which comprises of the two-phase spinel-rocksalt equilibrium, is calculated using the lever rule of thermodynamics, where the fraction of each phase is obtained from CALPHAD simulations.

In **Fig. 2B**, the vibrational entropy from the calculations above is smaller than the CALPHAD results of total entropy minus cation configurational entropy. The differences are likely due to an underestimation of the vibrational entropy: we assumed the harmonic approximation in vibrational entropy calculations; we did not strictly include the effect of lattice expansion with temperature; we did not fully eliminate imaginary modes. Other missing contributions to entropy (such as magnetic) also may account for the differences.

6. Synchrotron X-ray diffraction

The beamline 2-1 at Stanford Synchrotron Radiation Lightsource (SSRL) was used to obtain the high-resolution X-ray diffraction data of quenched materials. The powder was mixed with carbon black and diamond to reduce a self-absorption problem. An 0.5-mm diameter glass capillary from Charlessupper was used in this experiment. We used a Pilatus 100K detector and maintained the sample-to-detector distance at 700 mm. The energy of the X-rays was 17 keV and the spot size of the X-ray beam was 0.5 mm in height and 1 mm in width. We measured multiple 2-dimensional data while moving the detector over a 2-theta range of 6° to 62°. Multiple 2-dimensional images were merged and converted to theta versus intensity data with a Python script. The SRM 660b LaB6 reference material was measured together to calibrate the wavelength of the X-rays. We calculated the lattice parameter with a TOPAS6-academic program [29].

7. Oxide phase with good linearity of Gibbs energy with log p_{O_2}

A highly linear dependence of Gibbs energy (G) on $log_{10}\left(\frac{p_{O_2}}{p^0}\right)$ occurs for the rocksalt phase (but not the spinel phase) in Fe-Co-O, Fe-Ni-O, and Fe-Mg-O systems (**Figs. S9-S11**). When p_{O_2} varies, the change of G of rocksalt phase is accompanied with both cation redox and change of its oxygen to metal ratio. On the other hand, the spinel phase has (almost) no change in its oxygen-to-metal ratio and only slight cation redox occurs.

Using such linearity as a given condition and general solid-gas thermodynamic equilibrium relations, the derivation below finally gives a special relation between $ln\left(\frac{p_{O_2}}{p^0}\right)$ and solid-state oxygen stoichiometry x for a generic phase with formula MO_x. This derivation is more relevant to the rocksalt phase than the spinel.

The gas-phase oxygen chemical potential is $\mu_O^g = \mu_O^0 + \frac{1}{2}RTln(\frac{p_{O_2}}{p^0})$, where $\mu_O^0 = \frac{1}{2}G_{O_2}$ is the oxygen chemical potential of pure O_2 gas at reference pressure p^0 = 1 atm. The solid-phase oxygen chemical potential of a generic phase MO_x is $\mu_O^s = \frac{\partial G_{MO_x}}{\partial x}$.

In equilibrium, $\mu_O^g = \mu_O^s$, so $\frac{\partial G_{MO_x}}{\partial x} = \mu_O^0 + \frac{1}{2}RTln\left(\frac{p_{O_2}}{p^0}\right)$, and at constant temperature,

$$G_{MO_x}(x) = G_{MO_x}(x_0) + \int_{x_0}^{x} [\mu_O^0 + \frac{1}{2}RTln(\frac{p_{O_2}}{p^0})]du = G_{MO_x}(x_0) + \mu_O^0(x - x_0) + \frac{1}{2}RT$$

where *u* is the integration variable standing for the solid-state oxygen stoichiometry *x*.

Let $f(x) = ln\left(\frac{p_{O_2}}{p^0}\right)$ which is a material-dependent function that we are interested in, and similarly let $\int_0^x ln(\frac{p_{O_2}}{p^0})du = \int_0^x f(u)du = F(x)$ where *u* is again the integration variable. Then

$$G_{MO_x}(x) = G_{MO_x}(x_0) + \mu_O^0(x - x_0) + \frac{1}{2}RT[F(x) - F(x_0)] \quad (1)$$

On the other hand, the linear dependence of G_{MO_x} on $ln\left(\frac{p_{O_2}}{p^0}\right)$ can be expressed as

$$G_{MO_x}(x) = kf(x) + b \quad (2)$$

where *k* and *b* are constants.

By equations (1) and (2), we have $G_{MO_x}(x_0) + \mu_O^0(x - x_0) + \frac{1}{2}RT[F(x) - F(x_0)] = kf(x) + b$. Rearranging and letting *B* represent all the constant terms, we arrive at

$$\frac{1}{2}RTF(x) - kF'(x) + \mu_O^0 x = B$$

$$F'(x) - \frac{RT}{2k}F(x) = \frac{1}{k}(\mu_O^0 x - B)$$

Solving this differential equation, we obtain

$$F(x) = \frac{2RT\left(B - \mu_O^0 x\right) - 4k\mu_O^0}{R^2T^2} + Ce^{\frac{RT}{2k}x}$$

$$ln\left(\frac{p_{O_2}}{p^0}\right) = f(x) = F'(x) = C\frac{RT}{2k}e^{\frac{RT}{2k}x} - \frac{2\mu_O^0}{RT}$$

where *C* is a constant.

Here we see a double exponential relation between oxygen-to-metal stoichiometry *x* and $\left(\frac{p_{O_2}}{p^0}\right)$.

8. Tie line construction and maximal swing of phase fraction

To construct a tie line (common tangent) between curves of *G* for spinel and rocksalt phases vs. Fe ratio *y* (at a specific temperature and p_{O_2}), the total number of atoms that each curve represents must be the same and constant across all Fe ratios.

The rocksalt and spinel phases were set to each contain 1 mol of metal in the CALPHAD model. Since the oxygen-to-metal ratio (O/M) varies with Fe ratio *y* and differs between the two phases, a correction is required to give a constant total number of atoms for constructing a tie line.

Specifically, we subtracted the Gibbs energy of oxygen so that the tie line was constructed in an "Fe-Co binary" system. Namely, we use G(rocksalt, corrected) = G(rocksalt) - $(1/2)(O/M)_{rocksalt}G(O_2)$ and G(spinel, corrected) = G(spinel) - $(1/2)(O/M)_{spinel}G(O_2)$ to construct each tie line. In general, any correction that makes (O/M) constant would work equivalently.

The G(rocksalt, corrected) and G(spinel, corrected) were calculated at discrete values of the Fe ratio for both the CALPHAD model and the reduced model, because the $(O/M)_{spinel}$ and $(O/M)_{rocksalt}$ were given by CALPHAD model at discrete values of the Fe ratio. For the reduced model that fits the CALPHAD data reasonably well, shown by **Figs. S12-S14**, we used a spline interpolation of the discrete corrected G values to calculate tangent lines and the tie line. The tie line constructed for the reduced model is largely consistent with CALPHAD model. See representative results in **Figs. S15-S16**.

After we constructed tie lines for thermal reduction and CO_2 splitting conditions, we identified the four phase boundaries from which the optimal Fe ratio and the corresponding maximal swing of phase fraction can be determined using the method described in **Subsection 3 of Results and discussion**. Using sensitivity analysis, we varied each parameter of the reduced model independently and then constructed a new tie line , followed by calculation of new optimal Fe ratios and maximal phase fraction swings.

Supplementary Figures

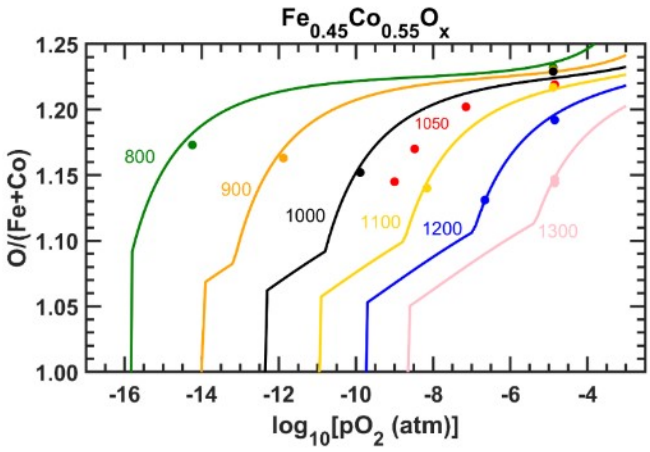

Fig. S1. Oxygen stoichiometry dependence on temperature and oxygen partial pressure (p_{O_2}) for an iron-poor ferrite $Fe_{0.45}Co_{0.55}O_{x_1}$**.** The curves are from CALPHAD simulations and the dots are from equilibrium measurements with a TGA. Each color indicates a temperature (in degrees Celsius).

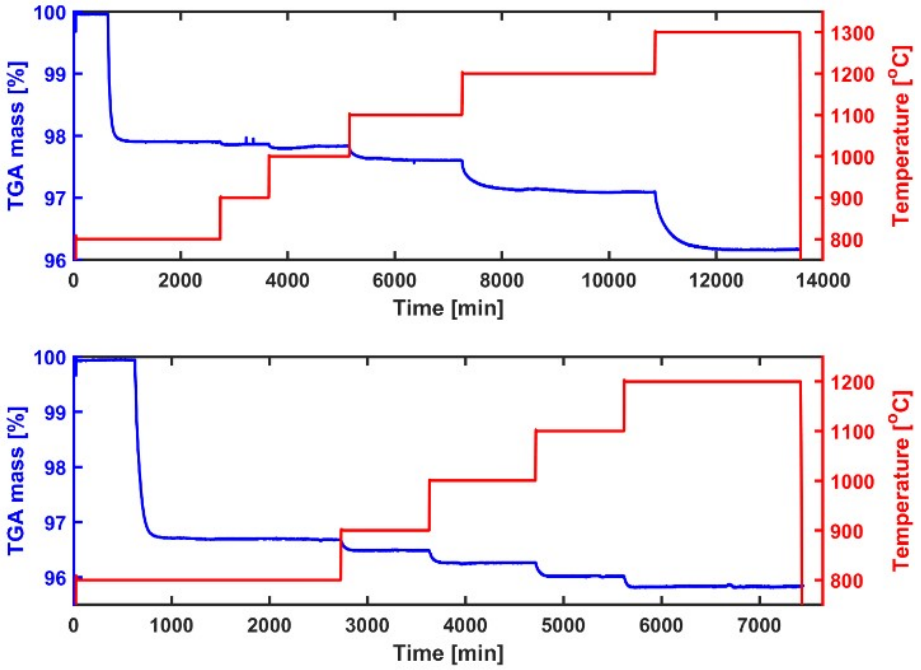

Fig. S2. Raw data of thermodynamic measurements of $Fe_{0.45}Co_{0.55}O_{x_1}$ using a TGA.

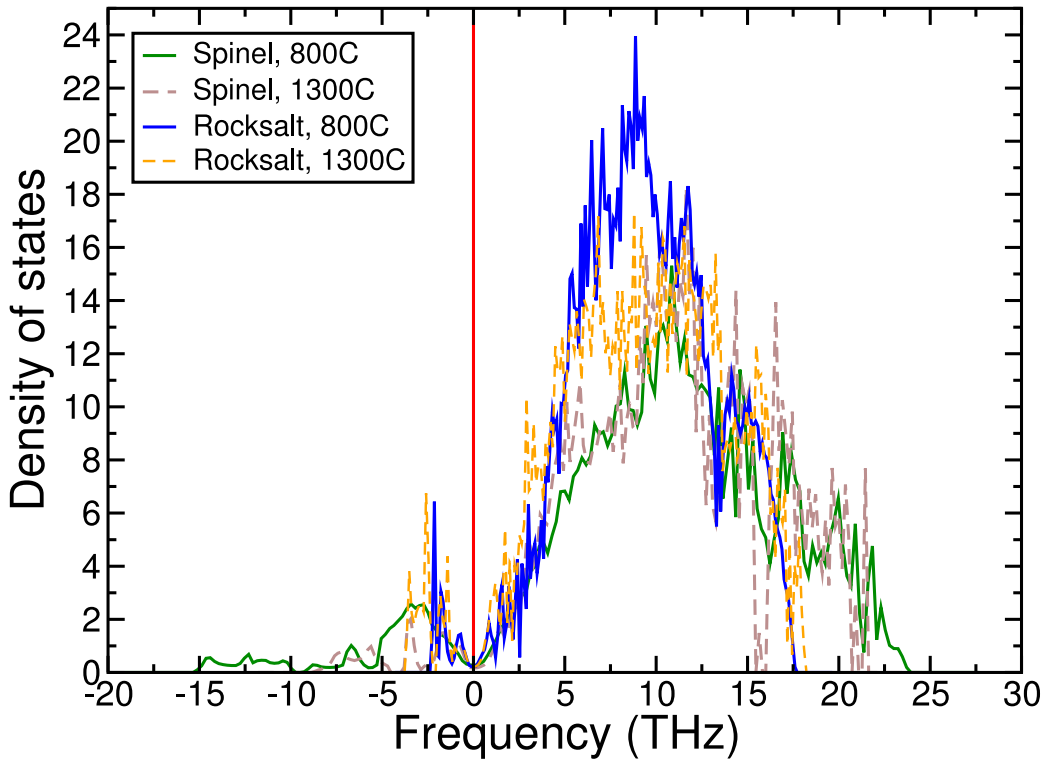

Fig. S3. Phonon density of states are plotted against the vibrational frequencies for spinel composition at 800 °C (solid green line), spinel at 1300 °C (dashed brown), rocksalt at 800 °C (solid blue), and rocksalt at 1300 °C (dashed orange). Negative frequencies indicate imaginary phonon modes.

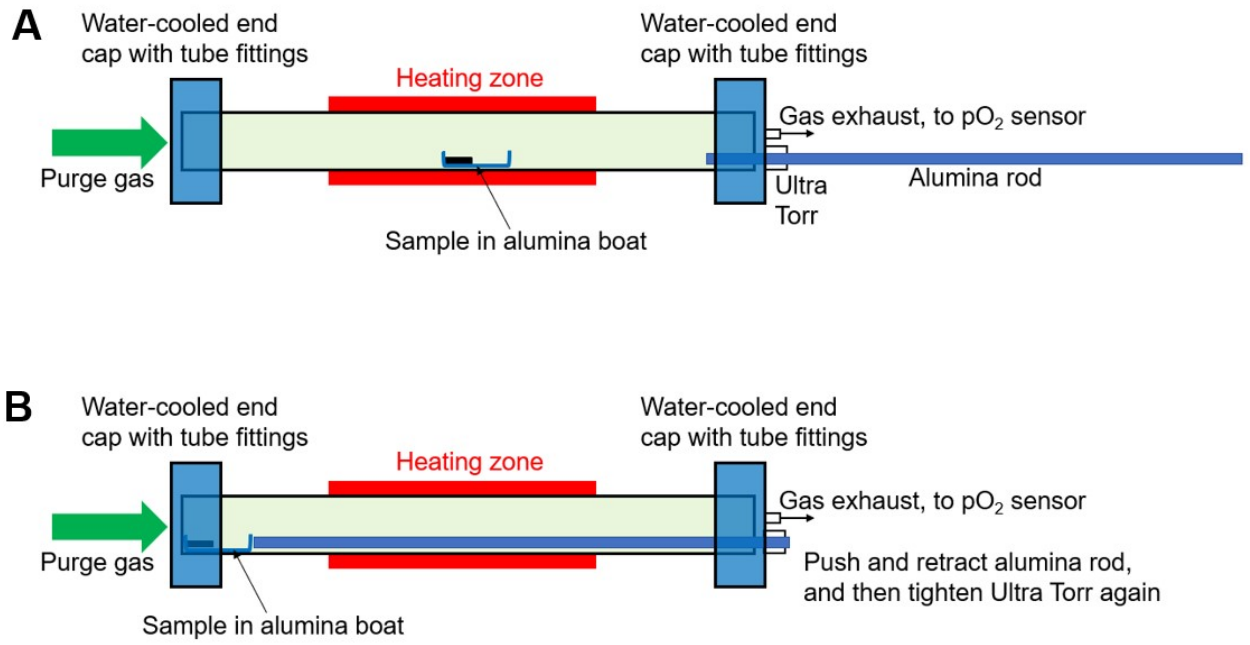

Fig. S4. Schematic of materials quenching system. Parts supporting the components are not drawn. (**A**) is the setup during reaction; (**B**) shows pushing the sample boat during quenching.

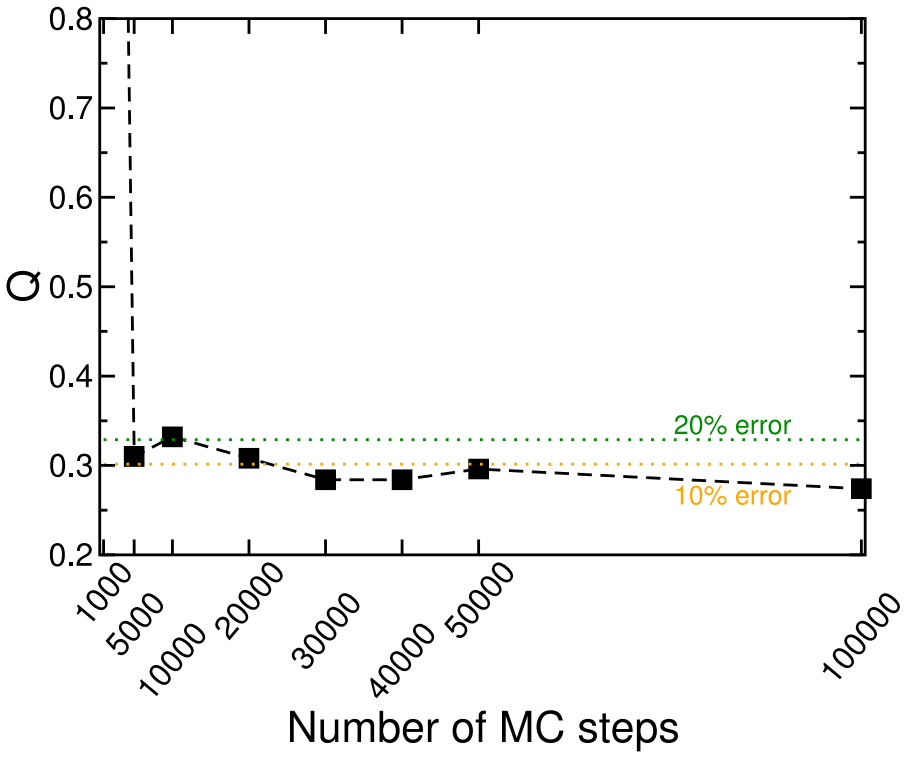

Fig. S5. Convergence of the similarity between the special quasirandom structure and an ideal random configuration (Q) with respect to number of steps in the Monte Carlo simulation. The dotted orange and green lines indicate 10% and 20% error of Q with respect to a Monte Carlo simulation with 100,000 steps.

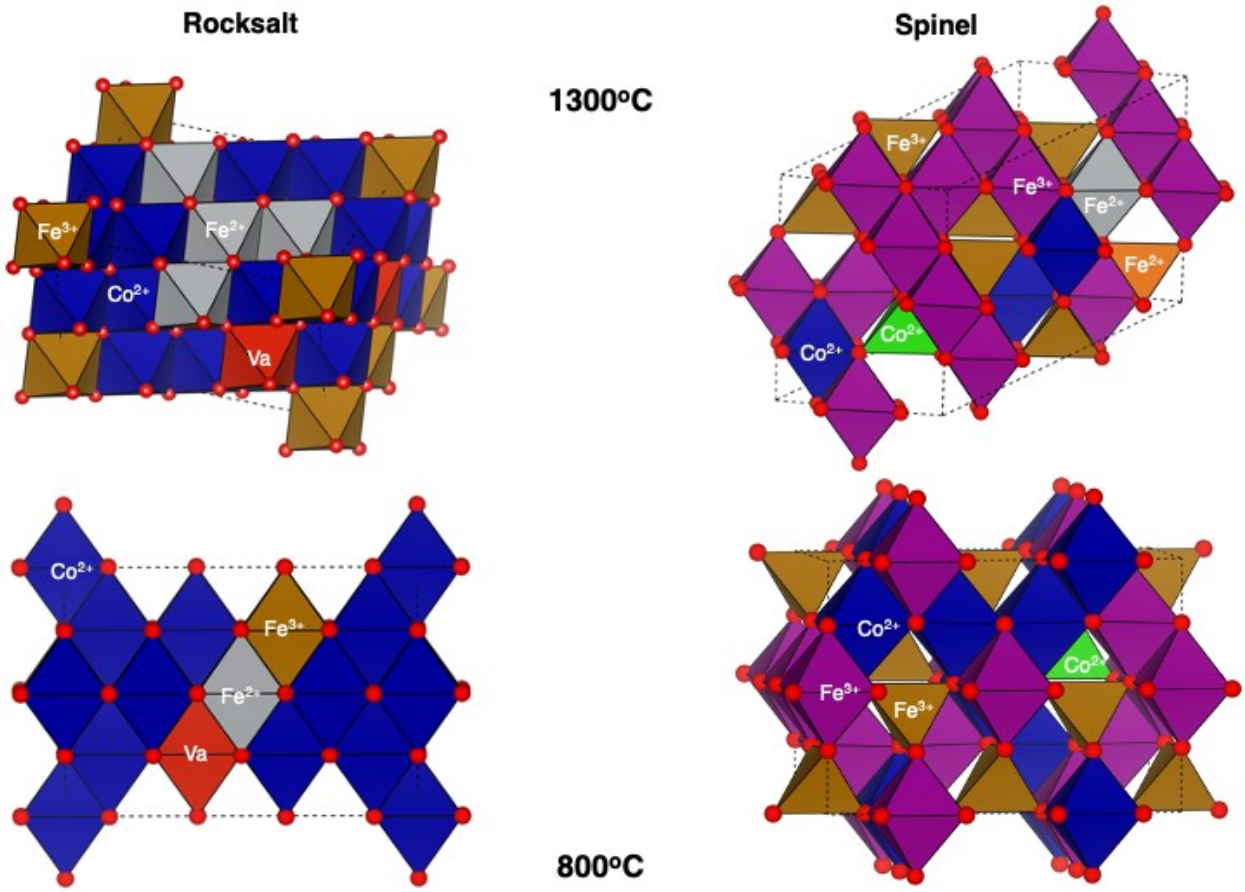

Fig. S6. Final special quasirandom structure models generated using Monte Carlo simulations for rocksalt (left panels) and spinel (right panels) phases. The top (bottom) two structures were generated for target compositions corresponding to 1300 °C and $pO_2 = 10^{-5}$ atm (800 °C and CO:CO_2 = 1:400 ($pO_2 = 10^{-13.25}$ atm)). Blue, brown/purple, grey, green, orange, and red polyhedra indicate octahedral Co^{2+}, octahedral/tetrahedral Fe^{3+}, octahedral Fe^{2+}, tetrahedral Co^{2+}, tetrahedral Fe^{2+}, and octahedral vacancies (Va), respectively.

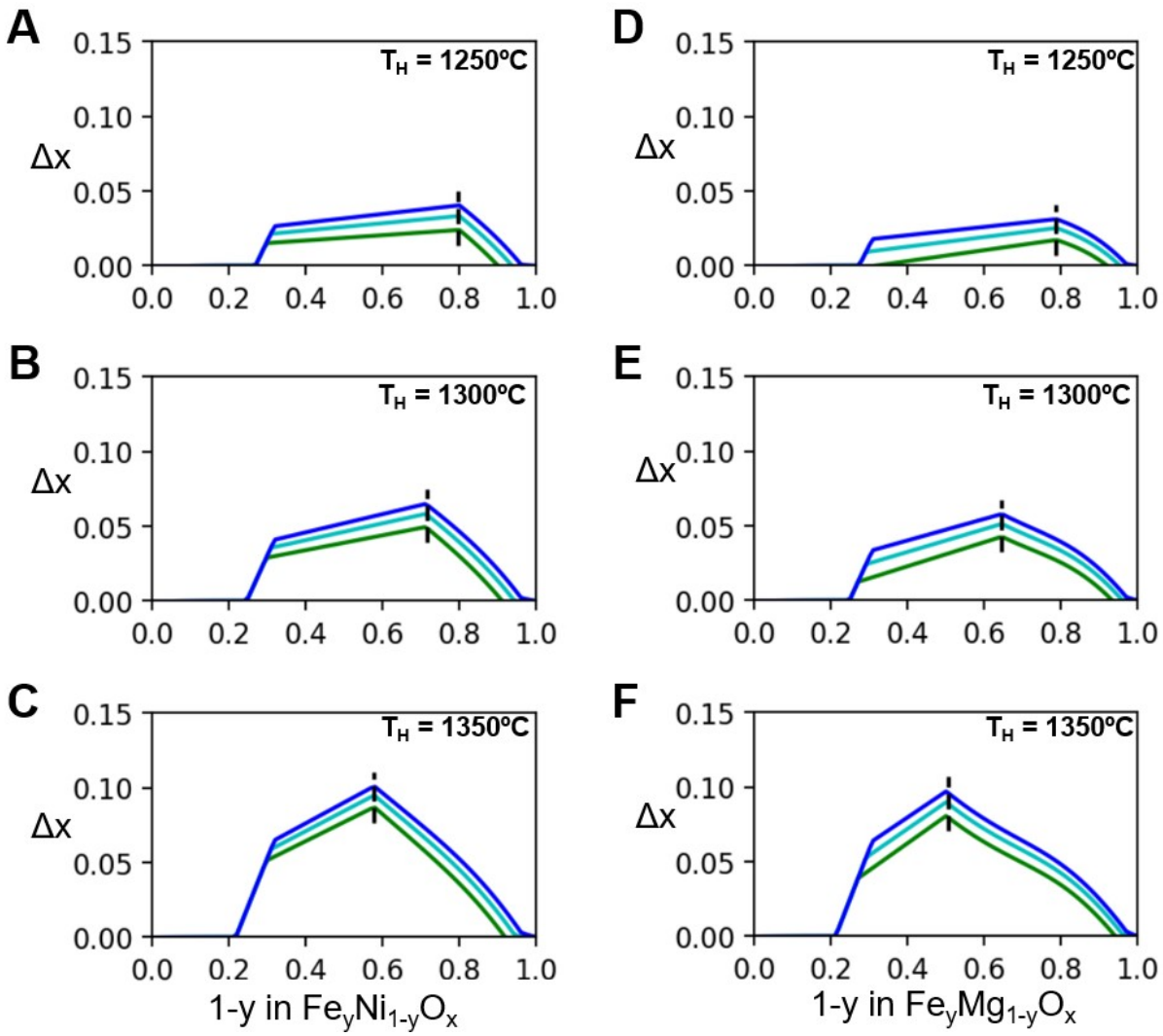

Fig. S7. Accurate prediction by phase diagram analysis of the optimal metal composition that maximizes the thermodynamic equilibrium capacity of ternary ferrites $Fe_yNi_{1-y}O_x$ (A-C) and $Fe_yMg_{1-y}O_x$ (D-F) in thermal reduction based thermochemical looping CO_2 splitting. Thermodynamic equilibrium CO_2 splitting capacities are represented by the change of oxygen stoichiometry, Δx, between thermal reduction and CO_2 splitting conditions. The vertical black dashed lines are the optimal metal compositions by the phase diagram analysis, which agree well with the peaks of the thermodynamic capacity curves. **A** and **D**, **B** and **E**, and **C** and **F** are for thermal reduction conditions of $p_{O_2} = 10^{-5}$ atm and T_H = 1250, 1300 and 1350 °C, respectively. T_L = 800 °C is for the CO_2 splitting step, and different CO_2-to-CO conversions are shown: the blue

line is for p_{O_2} = $10^{-11.49}$ atm ($CO:CO_2$ = 1:3000), the cyan line is p_{O_2} = $10^{-12.44}$ atm ($CO:CO_2$ = 1:1000), and the green line is p_{O_2} = $10^{-13.25}$ atm ($CO:CO_2$ = 1:400).

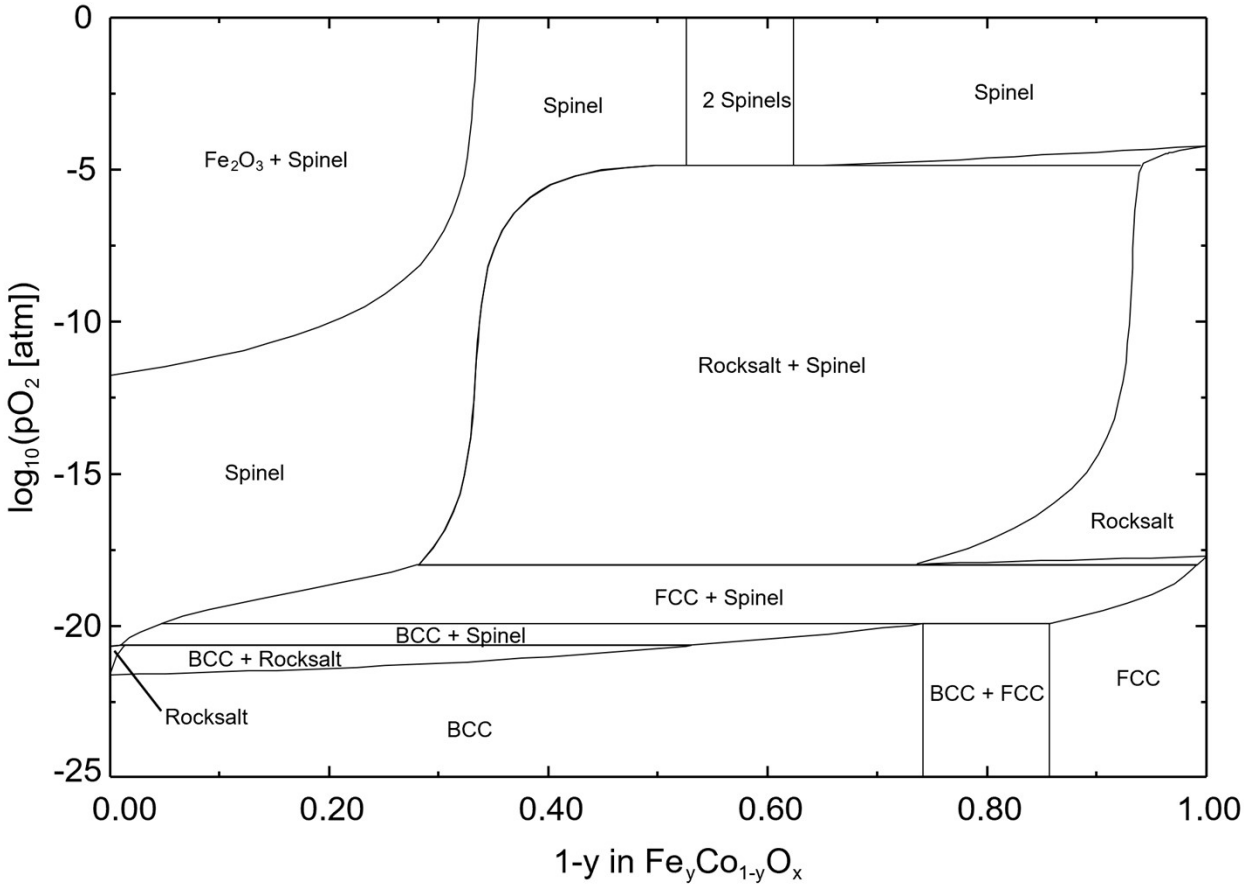

Fig. S8. Phase diagram of Fe-Co-O at 700°C according to CALPHAD. Metal phases (BCC, FCC) are merged in **Fig. 4A** for analysis purposes.

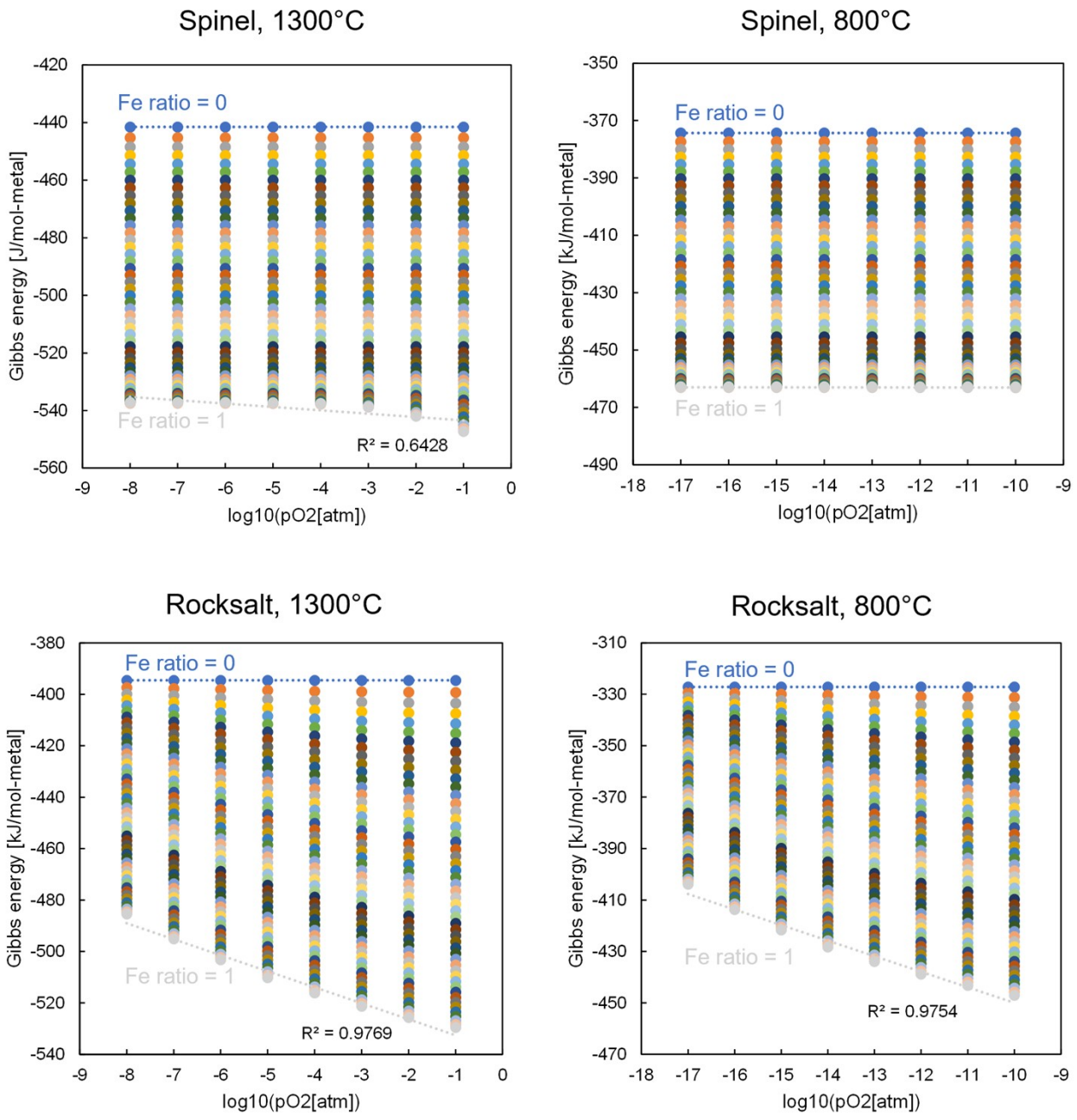

Fig. S9. Gibbs free energy (*G*) of rocksalt and spinel phases with $\log_{10}(p_{O_2})$ from CALPHAD simulations of the Fe-Co-O material system. The Fe ratio varies from 0 to 1 with an interval of 0.02. When the Fe ratio = 0, *G* of each phase does not change with p_{O_2} in the range considered. Dotted lines are linear fitting at a constant Fe ratio and thus unrelated to the reduced *G* model.

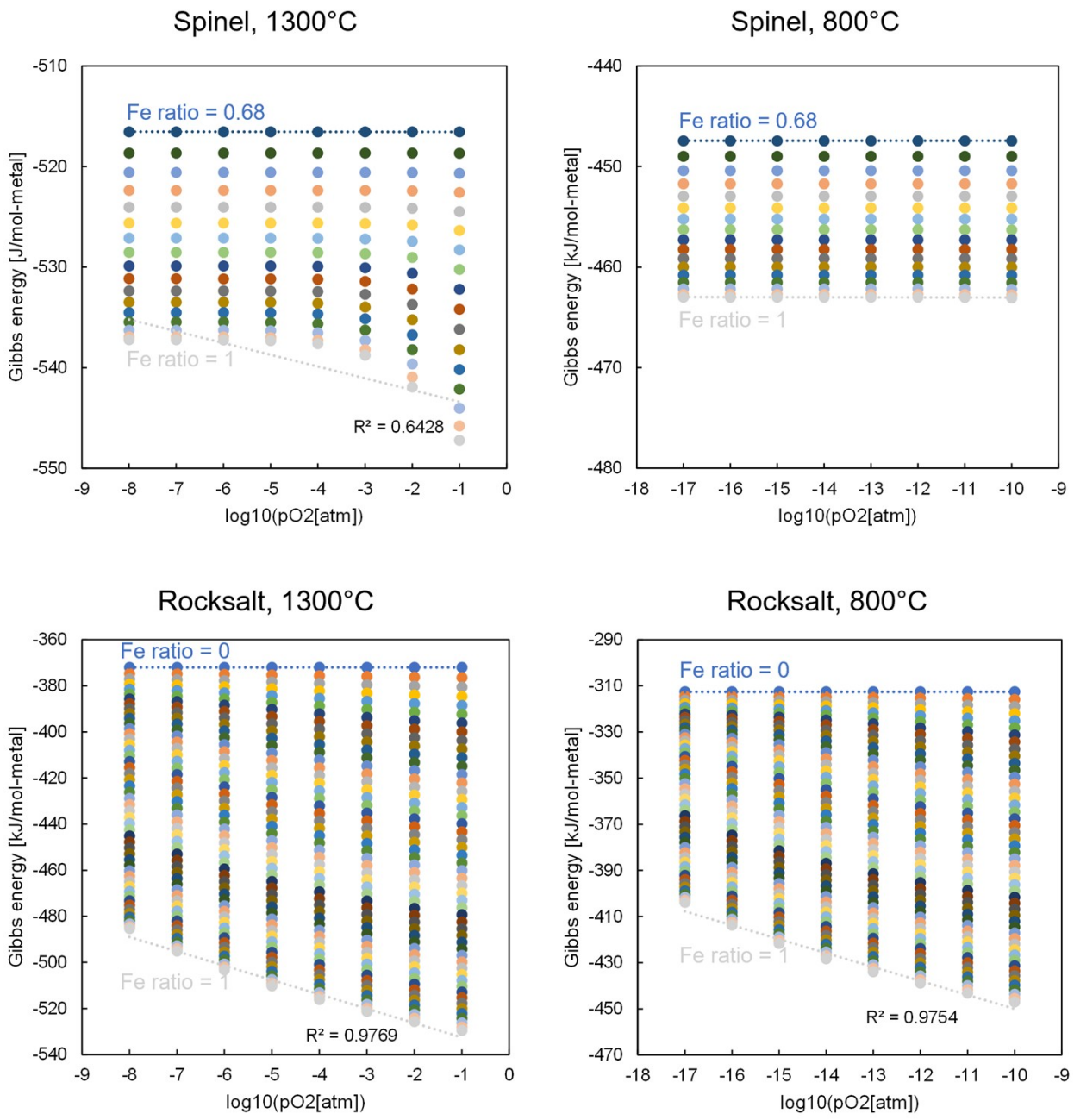

Fig. S10. Gibbs free energy (*G*) of rocksalt and spinel phases with $\log_{10}(p_{O_2})$ from CALPHAD simulations of the Fe-Ni-O material system. The Fe ratio varies from 0 to 1 with an interval of 0.02. When the Fe ratio = 0, *G* of the rocksalt phase does not change with p_{O_2} in the range considered. Dotted lines are linear fitting at a constant Fe ratio and thus unrelated to the reduced *G* model.

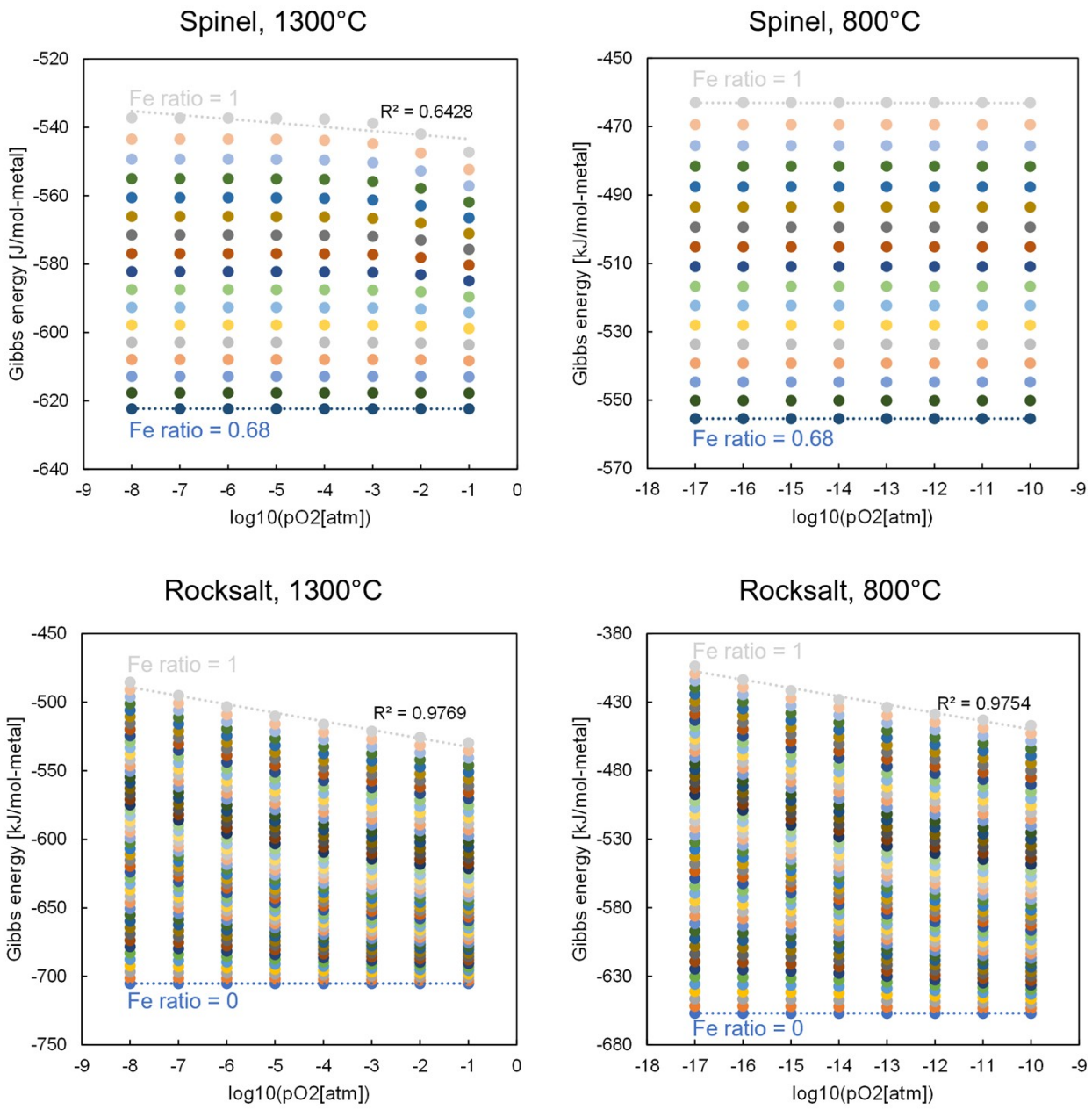

Fig. S11. Gibbs free energy (*G*) of rocksalt and spinel phases with $\log_{10}(^{p_{O_2}})$ from CALPHAD simulations of the Fe-Mg-O material system. The Fe ratio varies from 0 to 1 with an interval of 0.02. When the Fe ratio = 0, *G* of the rocksalt phase does not change with $^{p_{O_2}}$ in the range considered. Dotted lines are linear fitting at a constant Fe ratio and thus unrelated to the reduced *G* model.

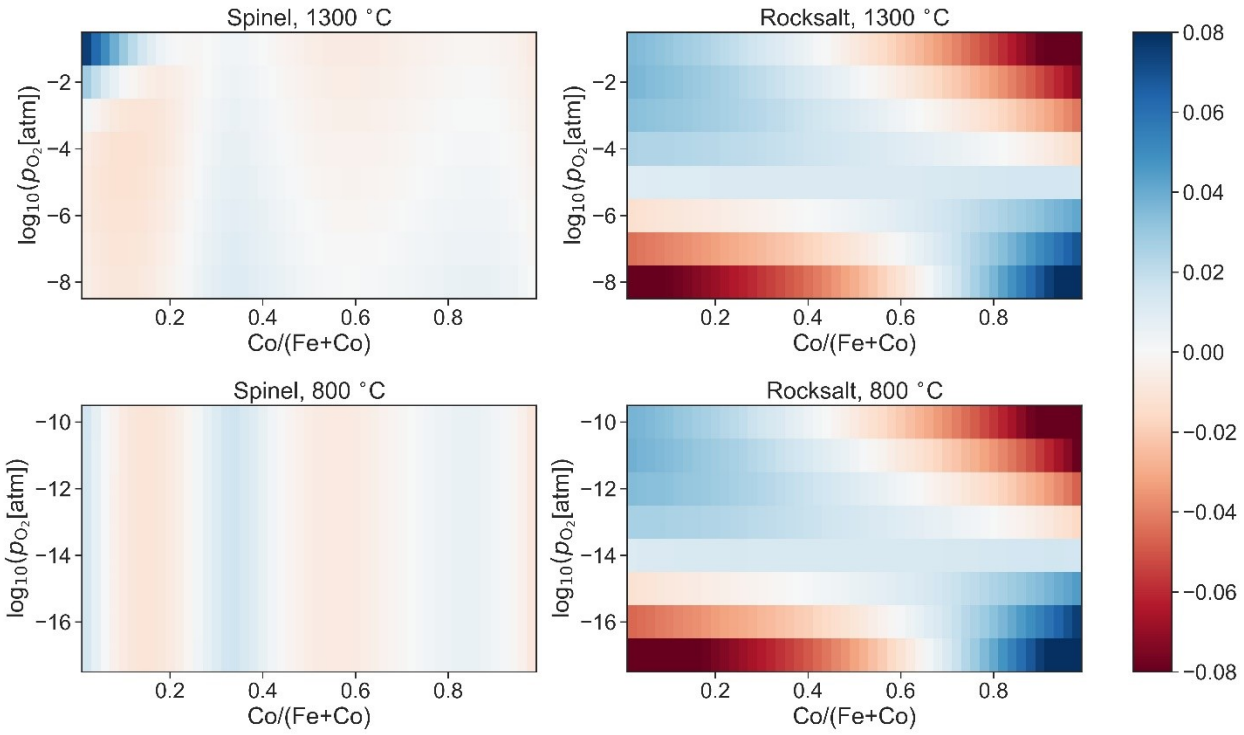

Fig. S12. Fitting error of the reduced Gibbs free energy (*G*) model of Fe-Co-O. The fitting error at each spot is defined as [G(reduced model) – G(CALPHAD)]/[range of G(CALPHAD) among the considered Co ratios and p_{O_2}], since generally the absolute *G* value is less meaningful than its variation.

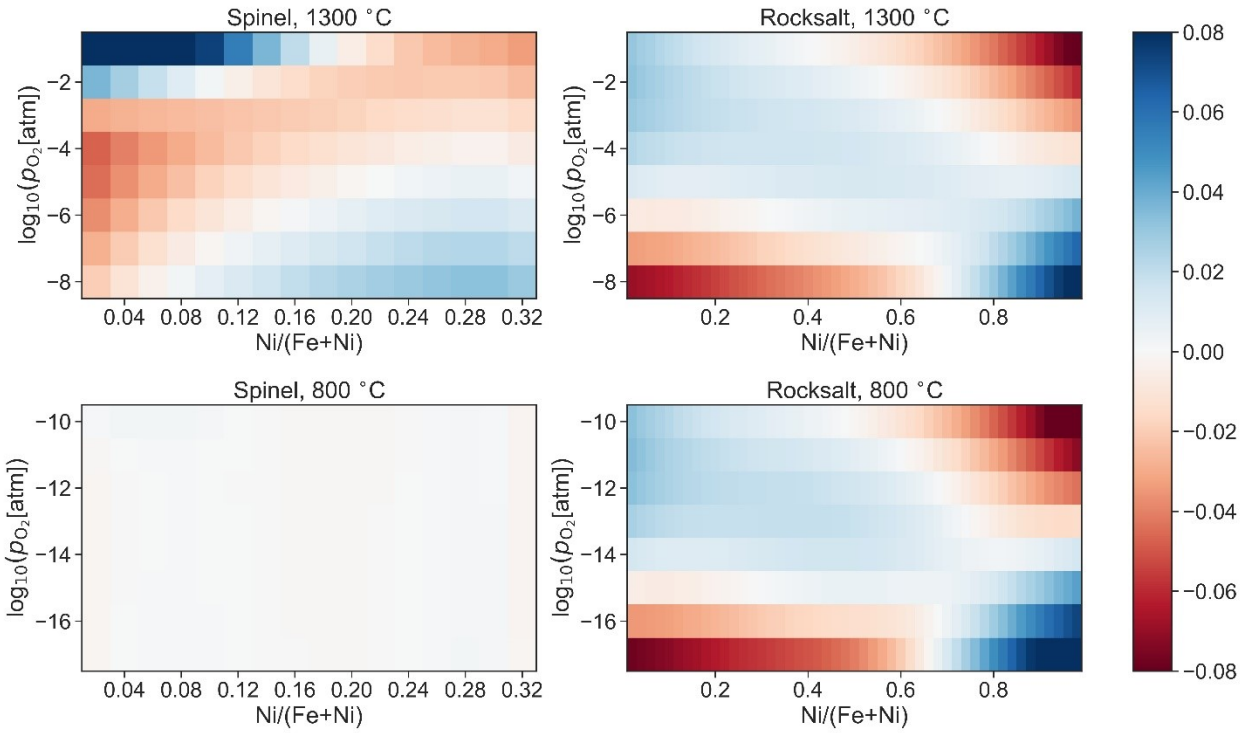

Fig. S13. Fitting error of the reduced Gibbs free energy (*G*) model of Fe-Ni-O. The fitting error at each spot is defined as [G(reduced model) – G(CALPHAD)]/[range of G(CALPHAD) among the considered Ni ratios and p_{O_2}], since generally the absolute *G* value is less meaningful than its variation.

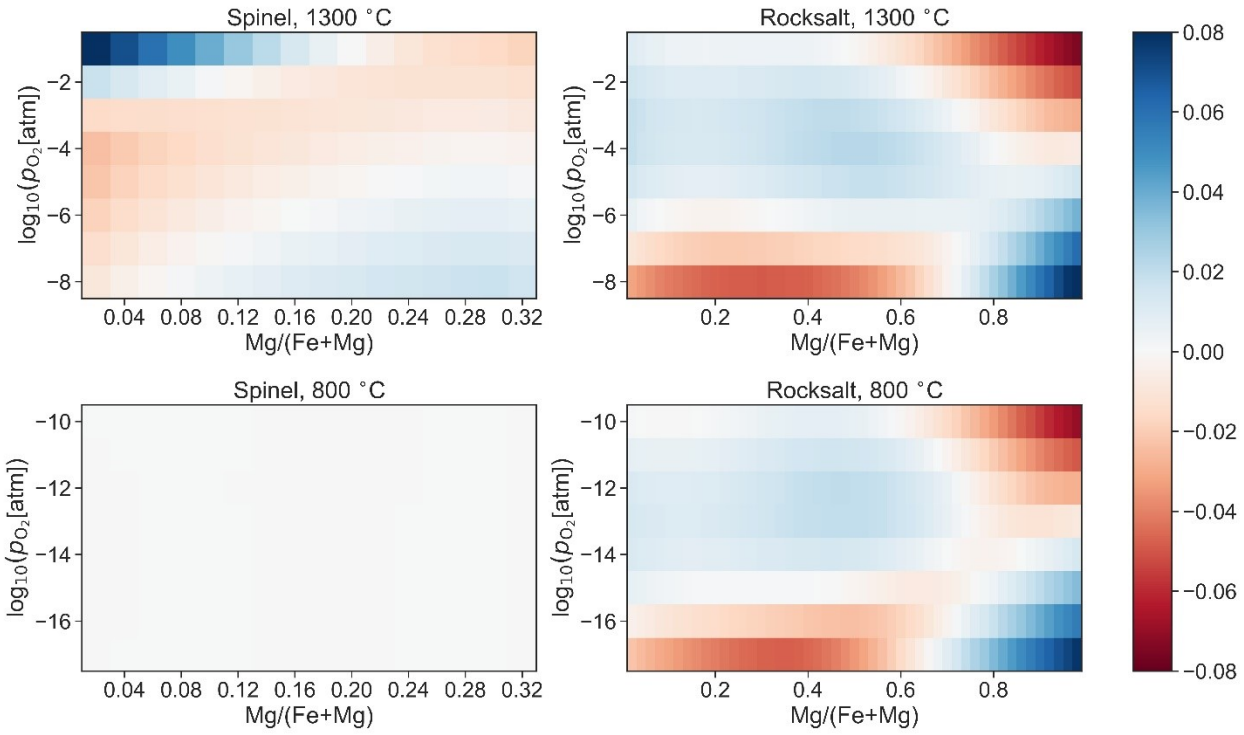

Fig. S14. Fitting error of the reduced Gibbs free energy (*G*) model of Fe-Mg-O. The fitting error at each spot is defined as [G(reduced model) – G(CALPHAD)]/[range of G(CALPHAD) among the considered Mg ratios and p_{O_2}], since generally the absolute *G* value is less meaningful than its variation.

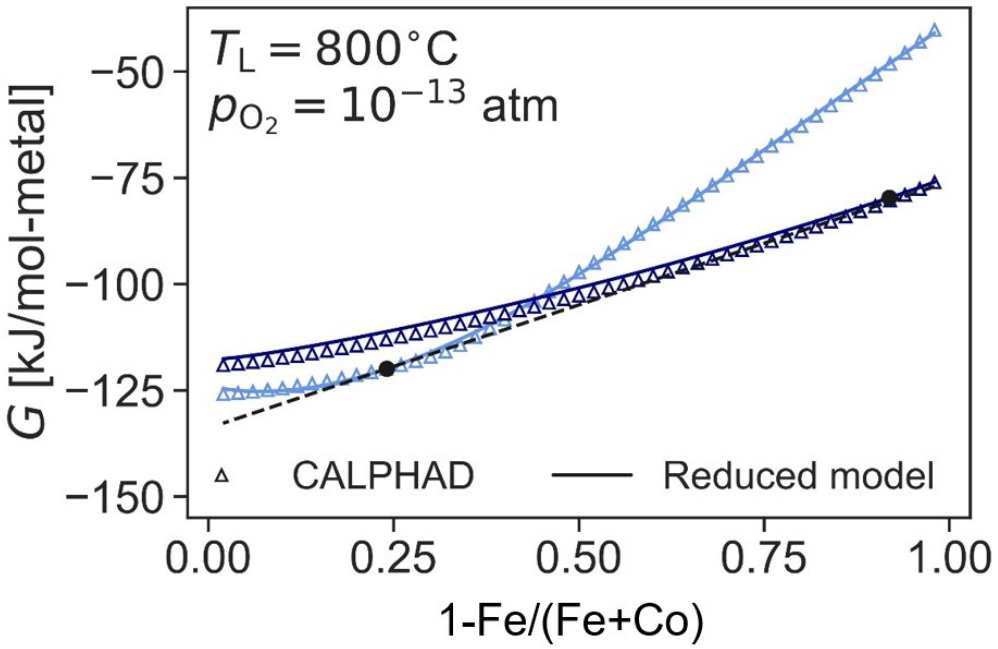

Fig. S15. Tie line construction between Gibbs energy (*G*) curves of spinel (light blue) and rocksalt (dark blue) for a representative CO_2 splitting condition. We applied a correction by subtracting the Gibbs energy of oxygen so that the total number of atoms is constant (see **Subsection 8 in Supplementary Text of ESI**). The triangles show the corrected *G*(CALPHAD) values while the curves show spline interpolations of the corrected *G*(reduced model). The black dashed line and dots indicate the tie line between the interpolation curves of the corrected *G*(reduced model).

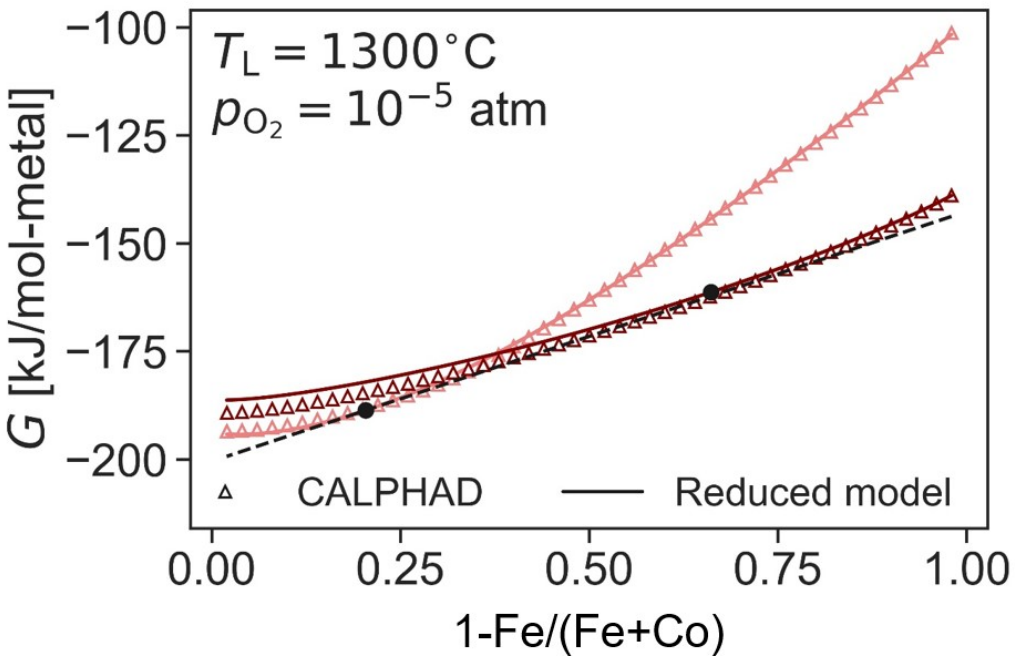

Fig. S16. Tie line construction between Gibbs energy (*G*) curves of spinel (light red) and rocksalt (dark red) for a representative thermal reduction condition. We applied a correction by subtracting the Gibbs energy of oxygen so that the total number of atoms is constant (see **Subsection 8 in Supplementary Text of ESI**). The triangles show the corrected *G*(CALPHAD) values while the curves show spline interpolations of the corrected *G*(reduced model). The black dashed line and dots indicate the tie line between the interpolation curves of the corrected *G*(reduced model).

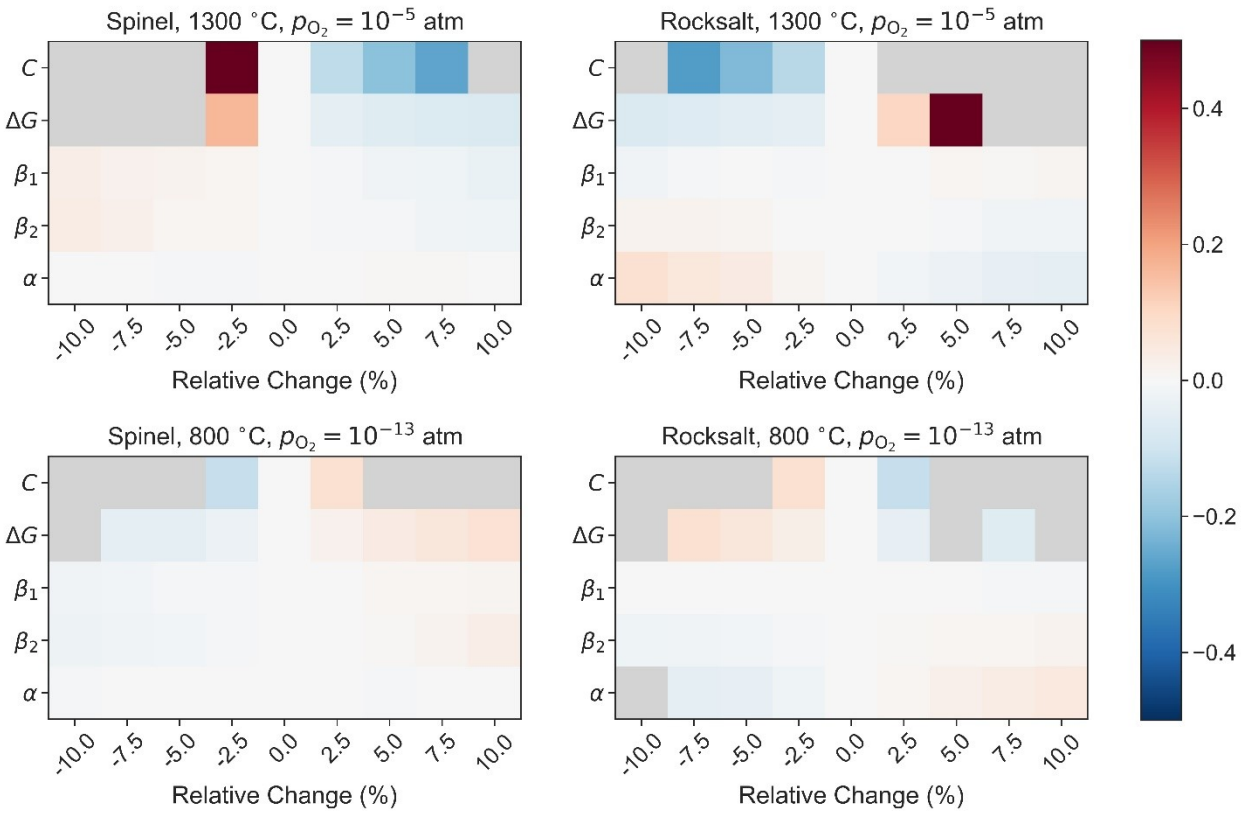

Fig. S17. Variations of the maximal phase fraction swing in thermal reduction based thermochemical looping cycle, when artificially changing each parameter of the reduced Gibbs free energy model for the Fe-Ni-O material system. The reaction conditions are thermal reduction at T_H = 1300 °C and p_{O_2} = 10^{-5} atm, and CO_2 splitting at T_L = 800 °C and p_{O_2} = 10^{-13} atm. Without artificial changes of any model parameter, the reduced *G* model gives the maximal phase fraction swing of 0.16 when the Fe ratio is 0.18. Grey boxes indicate that no common tangent tie line could be found for the *G* curves of rocksalt and spinel phases in those regions of model parameter changes.

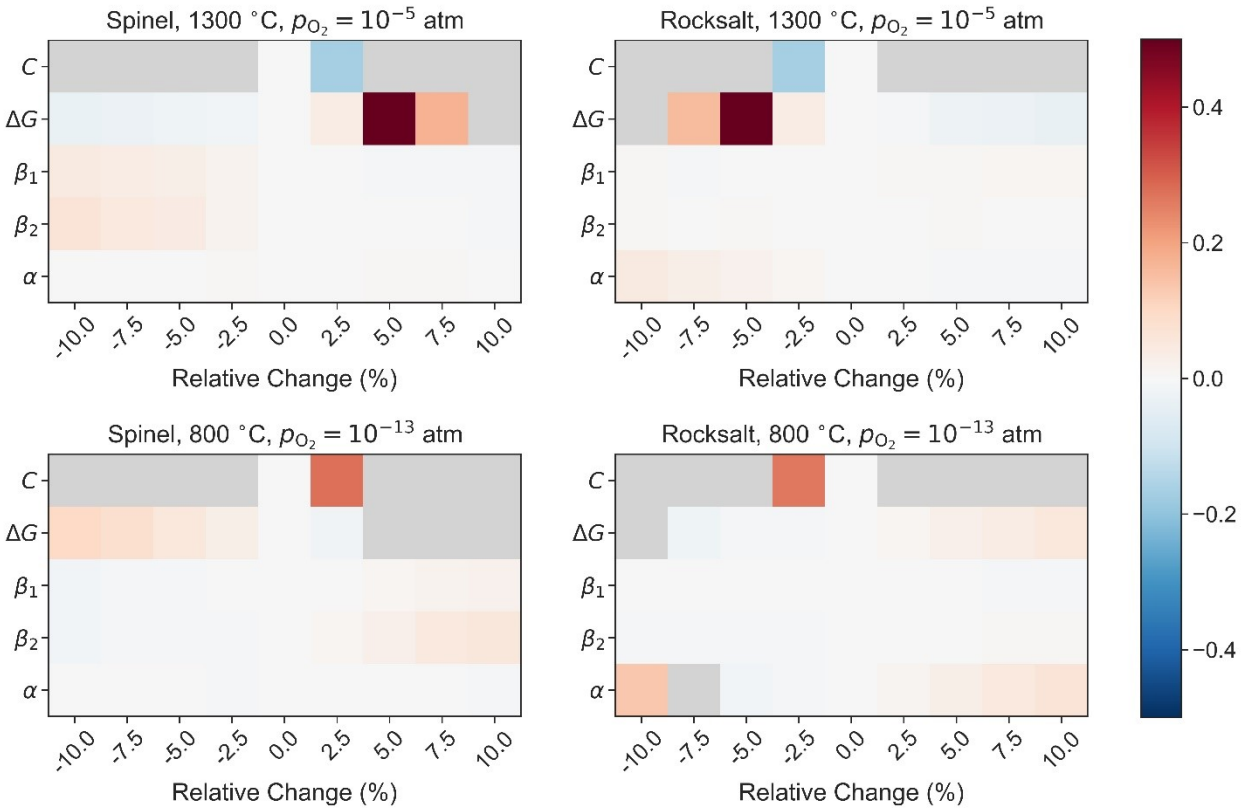

Fig. S18. Variations of the maximal phase fraction swing in thermal reduction based thermochemical looping cycle, when artificially changing each parameter of the reduced Gibbs free energy model for the Fe-Mg-O material system. The reaction conditions are thermal reduction at T_H = 1300 °C and p_{O_2} = 10^{-5} atm, and CO_2 splitting at T_L = 800 °C and p_{O_2} = 10^{-13} atm. Without artificial change of any model parameter, the reduced *G* model gives the maximal phase fraction swing of 0.08 when the Fe ratio is 0.73. Grey boxes indicate that no common tangent tie line could be found for the *G* curves of rocksalt and spinel phases in those regions of model parameter changes.

Supplementary Tables

Table S1. Inductively coupled plasma (ICP-OES) analysis of the bulk elemental ratios in quenched ferrites. Deviations of the measured Fe ratio from the nominal composition are within the experimental uncertainty.

Samples	ICP-OES results of molar ratio Fe/(Fe+Co)	
Nominal formula	Quenched from 1300 °C and p_{O_2} = 10^{-5} atm	Quenched from 800 °C and CO:CO_2 = 400:1
$Fe_{0.45}Co_{0.55}O_{x_1}$	0.4480	0.4483
$Fe_{2/3}Co_{1/3}O_{x_2}$	0.6731	0.6654

Table S2. Comparison of target compositions obtained from CALPHAD simulations and the resultant composition used in the SQS for the four rocksalts and spinels considered. y_X indicates the site fraction of species X in a given site. As CALPHAD simulations produced negligible Co^{3+} ion concentrations (occupancies vary between 10^{-4} and 0.013), we omitted these concentrations from the table. See **Subsection 5 in Supplementary Text of ESI** for details of constructing SQSs.

Condition	**Phase (site)**	**Source**	$y_{Fe^{2+}}$	$y_{Fe^{3+}}$	$y_{Co^{2+}}$	y_{Va}
1300 °C (Thermal reduction)	Rocksalt (octahedral)	CALPHAD	0.1676	0.1953	0.5393	0.0976
		SQS	0.1875	0.1875	0.5312	0.0938
	Spinel (tetrahedral)	CALPHAD	0.111	0.728	0.161	0.0
		SQS	0.125	0.750	0.125	0.0
	Spinel (octahedral)	CALPHAD	0.0671	0.6324	0.2970	5×10^{-6}
		SQS	0.0625	0.6250	0.3125	0.0
800 °C (CO_2 splitting)	Rocksalt (octahedral)	CALPHAD	0.0693	0.0976	0.7842	0.0488
		SQS	0.0938	0.0625	0.8125	0.0312
	Spinel (tetrahedral)	CALPHAD	0.030	0.846	0.123	0.0
		SQS	0.0	0.875	0.125	0.0
	Spinel (octahedral)	CALPHAD	0.0229	0.5764	0.4003	4×10^{-9}
		SQS	0.0	0.5625	0.4375	0.0

References for Electronic Supplementary Information

1 I.-H. Jung, S. A. Decterov, A. D. Pelton, H.-M. Kim and Y.-B. Kang, *Acta Mater.*, 2004, **52**, 507–519.

2 FactSage 8.0. Montreal, Canada., www.factsage.com.

3 I. H. Jung, S. A. Decterov and A. D. Pelton, *J. Phys. Chem. Solids*, 2004, **65**, 1683–1695.

4 I.-H. Jung, S. A. Decterov and A. D. Pelton, *Metall. Mater. Trans. B*, 2004, **35**, 877–889.

5 I.-H. Jung, S. A. Decterov and A. D. Pelton, *J. Phase Equilib. Diffus.*, 2004, **25**, 329–345.

6 S. Decterov, Y.-B. Kang and I.-H. Jung, *J. Phase Equilibria Diffus.*, 2009, 30, 443–461.

7 Y.-B. Kang and I.-H. Jung, *J. Phys. Chem. Solids*, 2016, **98**, 237–246.

8 B. Sundman and C. Gueneau, *State-of-the-art report on multi-scale modelling of nuclear fuels*, Paris, 2015.

9 G. Kresse and J. Hafner, *Phys. Rev. B*, 1993, **47**, 558–561.

10 G. Kresse and J. Furthmüller, *Phys. Rev. B*, 1996, **54**, 11169–11186.

11 P. E. Blöchl, *Phys. Rev. B*, 1994, **50**, 17953–17979.

12 G. Kresse and D. Joubert, *Phys. Rev. B*, 1999, **59**, 1758–1775.

13 G. Sai Gautam and E. A. Carter, *Phys. Rev. Mater.*, 2018, **2**, 95401.

14 O. Y. Long, G. Sai Gautam and E. A. Carter, *Phys. Rev. Mater.*, 2020, **4**, 45401.

15 V. I. Anisimov, J. Zaanen and O. K. Andersen, *Phys. Rev. B*, 1991, **44**, 943–954.

16 J. Sun, A. Ruzsinszky and J. P. Perdew, *Phys. Rev. Lett.*, 2015, **115**, 36402.

17 S. L. Dudarev, G. A. Botton, S. Y. Savrasov, C. J. Humphreys and A. P. Sutton, *Phys. Rev. B*, 1998, **57**, 1505–1509.

18 G. Sai Gautam, E. B. Stechel and E. A. Carter, *Adv. Theory Simulations*, 2020, **3**, 2000112.

19 G. Sai Gautam, E. B. Stechel and E. A. Carter, *Chem. Mater.*, 2020, **32**, 9964–9982.

20 C. G. Shull, W. A. Strauser and E. O. Wollan, *Phys. Rev.*, 1951, **83**, 333–345.

21 Y. Li, E. R. Maxey, J. W. Richardson and B. Ma, *Mater. Sci. Eng. B*, 2004, **106**, 6–26.

22 M. Gheisari, M. Mozaffari, M. Acet and J. Amighian, *J. Magn. Magn. Mater.*, 2008, **320**, 2618–2621.

23 A. Zunger, S.-H. Wei, L. G. Ferreira and J. E. Bernard, *Phys. Rev. Lett.*, 1990, **65**, 353–356.

24 M. Ångqvist, W. A. Muñoz, J. M. Rahm, E. Fransson, C. Durniak, P. Rozyczko, T. H. Rod and P. Erhart, *Adv. Theory Simulations*, 2019, **2**, 1900015.

25 A. van de Walle, P. Tiwary, M. de Jong, D. L. Olmsted, M. Asta, A. Dick, D. Shin, Y. Wang, L.-Q. Chen and Z.-K. Liu, *Calphad*, 2013, **42**, 13–18.

26 A. Togo, L. Chaput, I. Tanaka and G. Hug, *Phys. Rev. B*, 2010, **81**, 174301.

27 A. Togo and I. Tanaka, *Phys. Rev. B*, 2013, **87**, 184104.

28 A. Togo and I. Tanaka, *Scr. Mater.*, 2015, **108**, 1–5.

29 A. A. Coelho, *J. Appl. Crystallogr.*, 2018, **51**, 210–218.